

The HELLAS2XMM survey: IV. Optical identifications and the evolution of the accretion luminosity in the Universe. ^{*}

F. Fiore¹, M. Brusa^{2,6}, F. Cocchia^{1,3}, A. Baldi^{4,5}, N. Carangelo⁴, P. Ciliegi⁶, A. Comastri⁶, F. La Franca⁷, R. Maiolino⁸, G. Matt⁷, S. Molendi⁴, M. Mignoli⁶, G.C. Perola⁷, P. Severgnini⁹, C. Vignali^{10,6}

- ¹ INAF-Osservatorio Astronomico di Roma
via Frascati 33, Monteporzio-Catone (RM), I00040 Italy. e-mail: fiore@mporzio.astro.it
- ² Dip. di Astronomia Università di Bologna
- ³ Dip. di Fisica Università di Roma Tor Vergata
- ⁴ IASF/CNR Milano
- ⁵ Harvard-Smithsonian Center for Astrophysics
- ⁶ INAF-Osservatorio Astronomico di Bologna
- ⁷ Dip. di Fisica, Università Roma Tre
- ⁸ INAF-Osservatorio Astrofisico di Arcetri
- ⁹ INAF-Osservatorio Astronomico di Brera
- ¹⁰ Dept. of Astronomy and Astrophysics Pennsylvania State University

Received 22 April 2003 / Accepted 3 July 2003

Abstract. We present results from the photometric and spectroscopic identification of 122 X-ray sources recently discovered by XMM-Newton in the 2-10 keV band (the HELLAS2XMM 1dF sample). Their flux cover the range $8 \times 10^{-15} - 4 \times 10^{-13}$ erg cm⁻² s⁻¹ and the total area surveyed is 0.9 square degrees. One of the most interesting results (which is found also in deeper surveys) is that about 20% of the hard X-ray selected sources have an X-ray to optical flux ratio (X/O) ten times or more higher than that of optically selected AGN. Unlike the faint sources found in the ultra-deep Chandra and XMM-Newton surveys, which reach X-ray (and optical) fluxes more than one order of magnitude lower than the HELLAS2XMM survey sources, many of the extreme X/O sources in our sample have $R \lesssim 25$ and are therefore accessible to optical spectroscopy. We report the identification of 13 sources with $X/O \gtrsim 10$ (to be compared with 9 sources known from the deeper, pencil-beam surveys). Eight of them are narrow line QSO (seemingly the extension to very high luminosity of the type 2 Seyfert galaxies), four are broad line QSO. The results from our survey are also used to make reliable predictions about the luminosity of the sources not yet spectroscopically identified, both in our sample and in deeper Chandra and XMM-Newton samples. We then use a combined sample of 317 hard X-ray selected sources (HELLAS2XMM 1dF, Chandra Deep Field North 1Msec, Chandra SSA13 and XMM-Newton Lockman Hole flux limited samples), 221 with measured redshifts, to evaluate the cosmological evolution of the hard X-ray source's number and luminosity densities. Looking backward in time, the low luminosity sources ($\log L_{2-10keV} = 43 - 44$ erg s⁻¹) increase in number at a much slower rate than the very high luminosity sources ($\log L_{2-10keV} > 44.5$ erg s⁻¹), reaching a maximum around $z=1$ and then levelling off beyond $z=2$. This translates into an accretion driven luminosity density which is dominated by sources with $\log L_{2-10keV} < 44.5$ erg s⁻¹ up to at least $z=1$, while the contribution of the same sources and of those with $\log L_{2-10keV} > 44.5$ erg s⁻¹ appear, with yet rather large uncertainties, to be comparable between $z=2$ and 4.

Key words. X-ray: background, X-ray: surveys, QSO: evolution

1. Introduction

Hard X-ray observations are the most efficient way to discriminate accretion-powered sources, such as AGN, from starlight and optically thin hot plasma emission. Furthermore, hard X-rays are less affected than other bands by

^{*} based on observations collected at the European Southern Observatory, La Silla and Paranal, Chile, and at the Telescopio Nazionale Galileo, Roque de Los Muchachos, La Palma, TF - Spain. Based also on observations made with XMM-Newton, an ESA science mission. Table 1 is only available in electronic form at the CDS via anonymous ftp to [cdsarc.u-strasbg.fr](ftp://cdsarc.u-strasbg.fr) (130.79.128.5) or via <http://cdsweb.u-strasbg.fr/cgi-bin/qcat?J/A+A/>

obscuration. The advent of imaging instruments in the 2-10 keV band, first aboard ASCA and BeppoSAX (e.g. Ueda et al. 1999, Akiyama et al. 2000, Della Ceca et al. 1999, Fiore et al. 1999,2001, La Franca et al. 2002, Giommi et al. 2000) and then on Chandra and XMM-Newton, has led to a dramatic advance. Deep surveys have resolved 80-90% of the 2-10 keV Cosmic X-ray Background (CXB, see e.g. Mushotzky et al. 2000, Giacconi et al. 2001,2002, Brandt et al. 2001, Hasinger et al. 2001), and the detailed study of the cosmic evolution of the hard X-ray source population is being pursued combining deep and shallow Chandra and XMM-Newton surveys. These studies confirm, at least qualitatively, the predictions of standard AGN synthesis models for the CXB (e.g. Setti & Woltjer 1989, Comastri et al. 1995, 2001): the 2-10 keV CXB is mostly made by the superposition of obscured and unobscured AGN. Quantitatively, though, rather surprising results are emerging: a rather narrow peak in the range $z=0.7-1$ is present in the redshift distributions from ultra-deep Chandra and XMM-Newton pencil-beam surveys (e.g. Barger et al. 2001,2002, Cowie et al. 2003, Hasinger 2003), in contrast to the broader maximum observed in previous shallower soft X-ray surveys (e.g. ROSAT, Schmidt et al. 1998, Lehmann et al. 2001) and predicted by the above mentioned synthesis models; furthermore, evidence is emerging (related to the difference above) of a luminosity dependence in the number density evolution of both soft and hard X-ray selected AGN (Cowie et al. 2003, Hasinger 2003).

The ultra-deep Chandra and XMM-Newton surveys of the Chandra Deep Field North (1Msec, CDFN, Brandt et al. 2001), Chandra Deep Field South (CDFN, Giacconi et al. 2002) and Lockman Hole (LH, Hasinger et al. 2001) cover each about 0.05-0.1 square degrees. For this reason the number of high luminosity sources in these surveys is small (the slope of the AGN luminosity function at high luminosities is very steep). As an example, in the CDFN there are only 6 AGN with $\log L_{2-10keV} \gtrsim 44$ at $z > 3$ and 20 at $z > 2$ (Cowie et al. 2003). To compute an accurate luminosity function on wide luminosity and redshift intervals, and to find sizeable samples of “rare” objects, such as high luminosity, highly obscured type 2 QSO (and also of other rare sources like the X-ray bright, optically normal galaxies, XBONGs, Fiore et al. 2000, Comastri et al. 2002) a much wider area needs to be covered, of the order of a few square degrees. To this purpose we are carrying out the HELLAS2XMM serendipitous survey, using suitable XMM-Newton archive observations (Baldi et al. 2002). The HELLAS2XMM survey goal is to cover ~ 4 square degrees using 20 XMM-Newton fields. The majority of them share a Chandra coverage, which, thanks to the higher angular resolution, helps in the process of optical identification (see Brusa et al. 2003). The survey will consist of about 500 sources selected in the 2-10 keV band. Among them, we expect at least 100 highly obscured AGN, a number sufficient to evaluate their luminosity function and evolution up to $z=2-3$ with a level of statistical accuracy adequate for a meaningful comparison with those of the unobscured AGN.

As an intermediate step, in this paper we present the results of the optical identification of 122 hard X-ray selected sources detected in five XMM-Newton fields (PKS0312-77, PKS0537-28, A2690, G158-100, Markarian 509), covering a total of 0.9 square degrees (hence the acronym ‘1dF’ for this sample), and of 0.4 square degree at $F_{2-10keV} = 2 \times 10^{-14}$ erg cm $^{-2}$ s $^{-1}$, where $\sim 40\%$ of the CXB is resolved in discrete sources). The optical photometric and spectroscopic observations of the sources in the other 20 fields is in progress. The five XMM-Newton fields have been studied using the ESO 3.6m and VLT/UT1 telescopes and the TNG telescope. For all the 122 X-ray sources we have complete photometric coverage down to $R \sim 25$ and nearly complete spectroscopic coverage down to $R=24$ (90%). We combine the results on the optical identification of the HELLAS2XMM 1dF sources with those from the CDFN, Chandra SSA13 (Mushotzky et al. 2000, Barger et al. 2001), and XMM-Newton Lockman Hole fields to evaluate the evolution of the hard X-ray selected AGN number and luminosity density up to $z=2-3$. The combined sample consists of 317 hard X-ray selected sources spanning the flux range $10^{-15} - 4 \times 10^{-13}$ erg cm $^{-2}$ s $^{-1}$. The fraction of sources with measured redshift is 70%.

The paper is organized as follows: Sects. 2 and 3 present the results of the optical photometric and spectroscopic identifications of the HELLAS2XMM 1dF source sample; Sect. 4 compares the HELLAS2XMM 1dF sample with other samples of hard X-ray sources from deeper Chandra and XMM-Newton survey; Sect. 5 discusses the population of sources with high X-ray to optical flux ratio. We show here how the results obtained using the HELLAS2XMM 1dF sample can be used to make statistical predictions about this population of sources at fainter X-ray (and optical) fluxes; Sect. 6 presents our results on the evolution of the X-ray source’s number and luminosity density; finally Sect. 7 discusses our main findings. A $H_0 = 70$ km s $^{-1}$ Mpc $^{-1}$, $\Omega_M=0.3$, $\Omega_\Lambda = 0.7$ cosmology is adopted throughout.

2. Optical identifications

We have obtained relatively deep ($R=24-25$) optical images for all 122 hard X-ray sources in the HELLAS2XMM 1dF sample using EFOOSC2 at the ESO 3.6m telescope and DOLORES at the TNG. Exposures were typically of 10m per image. Optical frames and X-ray images were brought to a common astrometric reference frame using bright AGN (from 5 to 15 AGN per field). Typical systematic shifts were of the order of $1''$, the maximum shift was of $\sim 2''$.

Images were bias subtracted, flat field divided, and flux calibrated using observations of standard stars acquired during each night. Source detection was performed using the SExtractor package (Bertin et al. 2000). Additional $3''$

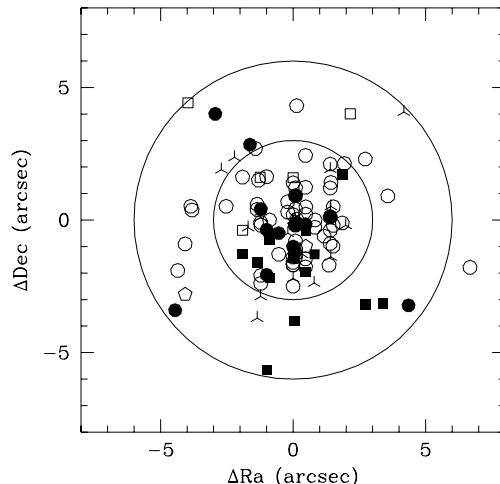


Fig. 1. The displacement between the X-ray position and the position of the nearest optical counterpart for the HELLAS2XMM 1dF sample sources. Open circles = broad line AGN; filled circles = narrow line AGN; filled squares = emission line galaxies; open squares = normal galaxies; stars = stars; pentagons = clusters of galaxies; skeleton triangles = unidentified objects. The two circles have radii of 3 and 6 arcseconds.

diameter aperture photometry was performed on the R band images at the position of eight bright K band sources (Mignoli et al. 2003).

We found optical counterparts brighter than $R \sim 25$ within $\sim 6''$ from the X-ray position in 116 cases (actually within $3''$ for $\sim 80\%$ of the cases, see Fig. 1). The average displacement between the X-ray positions and the positions of the optical counterparts is of $2.1'' \pm 1.5''$. This is consistent with what found in other XMM-Newton surveys (Barcons et al. 2002, Hasinger et al. 2001). Six X-ray sources have optical counterparts fainter than $R \sim 24$ (5%).

Two of the sources with optical counterpart (PKS0312_8 and A2690_13) are more extended than the XMM-Newton/EPIC Point Spread Function at their off-axis angles (Ghizzardi 2001). Their X-ray emission is probably due to intracluster or intragroup hot, optically thin, plasma emission. For another source (PKS0537_37) several relatively bright galaxies are present around the X-ray error-box. Also in this case the X-ray emission is probably due to intracluster or intragroup gas. These three sources will therefore be excluded when studying the evolution of the accretion luminosity

Table 1 gives for each source the X-ray position, the position of the optical counterpart, the displacement between the X-ray and optical positions, the X-ray flux, the R magnitude of the optical counterpart (or the three σ upper limit), the classification of the optical spectrum, the redshift and the X-ray luminosity.

3. Optical spectroscopic redshifts and classification

Optical spectra of 97 of the 110 sources with optical counterparts brighter than $R=24$ have been obtained using EFOSC2 @ the ESO 3.6m telescope and FORS1 @ VLT/UT1 during 5 observing runs performed between Jan. 2000 and Aug. 2002. A total of 9 nights at the 3.6m and 24 hours of VLT time have been devoted to this program.¹

Long slit spectroscopy has been carried out in the 3800-10000 Å band with resolution between 7 and 13 Å. Data reduction was performed using both the MIDAS (Banse et al. 1983) and IRAF² packages. Wavelength calibrations were carried out by comparison with exposures of He-Ar, He, Ar and Ne lamps. The flux calibration of the spectra was obtained using observations of spectro-photometric standard stars (Oke, 1990), performed within a few hours from the object's spectroscopy.

For 93 sources the optical spectroscopy produced reliable redshifts. In the four remaining cases the redshift determination is tentative, based on a faint, single line.

¹ six sources have counterparts with R between 24 and 25, still accessible to VLT spectroscopy, but demanding exposure times too long for the time allocated to our VLT run

² IRAF is distributed by the National Optical Astronomy Observatories, which is operated by the Association of Universities for Research in Astronomy, Inc., under cooperative agreement with the National Science Foundation

3.1. Source breakdown

In the majority of the cases optical spectra are of sufficiently good quality to allow a reliable classification of the optical counterpart. Objects with permitted emission lines broader than 2000 km/s (FWHM) are identified with type 1 AGN; objects with permitted emission lines narrower than 2000 km/s are classified as type 2 AGN, if they possess strong [OIII], NeV, MgII, or CIV emission lines, or as Emission Line Galaxies (ELGs) if they possess strong [OII] or H α emission lines. In six cases the presence of broad emission lines in the optical spectrum cannot be excluded, due to the insufficient quality of the spectrum and the classification of the object is therefore uncertain (see notes in Table 1). Objects without strong emission lines (equivalent width $EW < 5 - 8 \text{ \AA}$) but with stellar absorption lines and a red continuum are classified as Early Type Galaxies (ETGs).

In four cases there are two candidate counterparts inside the X-ray error-box (see notes in Table 1) which could both contribute to the detected X-ray emission. In two cases the counterparts are at the same redshift and are both emission line galaxies, hence the X-ray luminosity is univocally determined, of course within a factor of two. In one case the two counterparts are a galaxy and a type 1 AGN, which is therefore adopted as the most likely counterpart. The last case, PKS0312_35, is rather intriguing: both a type 1 QSO and an extremely red object, R-K > 6.6, which is also a 0.4mJy (at 5GHz) radio source, see Brusa et al. (2003), are present in the error-box. In the following we shall adopt as counterpart the type 1 QSO.

The source breakdown therefore includes: 61 broad line QSO and Seyfert 1 galaxies; 14 narrow line AGN (9 of which have $\log L_{2-10keV} > 44 \text{ erg s}^{-1}$, see next Sect. for details on luminosity determination, and can therefore be considered type 2 QSO); 14 emission line galaxies, all with $\log L_{2-10keV} > 42.7$ and therefore all probably hosting an AGN; 5 early type galaxies with $41.9 < \log L_{2-10keV} < 43.0$, therefore XBONGs, all probably hosting an AGN; 1 star; 2 groups or clusters of galaxies.

In summary, 94 of the 97 sources with optical spectroscopy are associated with AGN emission, the majority (63%) are type 1 AGN.

A more detailed discussion of the optical spectra of all objects is deferred to another publication. In the following we limit ourselves to consider two broad categories: *optically unobscured AGN*, i.e. type 1, broad emission line AGN, and *optically obscured AGN*, i.e. AGN whose nuclear optical emission, is totally or strongly reduced by dust and gas in the nuclear region and/or in the host galaxy.

4. The HELLAS2XMM 1dF sample in a context: comparison with deeper Chandra and XMM-Newton surveys

In the following Sects. we shall also use results from three additional hard X-ray samples:

1- Chandra Deep Field North sample from Barger et al. (2002): 88 sources with $F_{2-10keV} > 10^{-15} \text{ erg cm}^{-2} \text{ s}^{-1}$ in the inner 6.5 arcmin radius region plus 32 sources with $F_{2-10keV} > 5 \times 10^{-15} \text{ erg cm}^{-2} \text{ s}^{-1}$ in the annulus between 6.5 and 10 arcmin radii, for a total of 120 sources (67 with a spectroscopic redshift).

2- Lockman Hole sample: 55 sources in the inner 12 arcmin radius region. Fluxes are from Baldi et al. (2002), optical identifications are from Mainieri et al. (2002), for a total of 55 sources, 44 already identified (41 spectroscopic redshifts and 3 photometric redshifts);

3- SSA13 sample from Mushotzky et al. (2000) and Barger et al (2001): 20 sources with $F_{2-10keV} > 3.8 \times 10^{-15} \text{ erg cm}^{-2} \text{ s}^{-1}$ in a 4.5 arcmin radius region, 13 with spectroscopic redshift.

Overall, we shall deal with 317 hard X-ray selected sources from Chandra and XMM-Newton surveys, 221 (70%) of them identified with an optical counterpart whose redshift is available. Five of these sources are identified with groups or cluster of galaxies, two with stars. We shall not consider in the following these seven sources. It is highly unlikely that other stars are present among the sources without a redshift. It is also unlikely that other groups or clusters of galaxies are present among the sources without an optical counterpart (nine in the whole combined sample), because the X-ray sources do not present any evidence of extension. In the following we shall assume that no other star, group or cluster of galaxy is present among the sources without a redshift and limit the analysis to the 310 sources probably hosting an active nucleus.

Classification of the optical spectra from the additional samples are adopted from the above publications, when available. Otherwise, we produced a tentative classification by visual inspection of the published optical spectra (Barger et al. 2001,2002), adopting the criteria in Sect. 3.1.

The combined sample includes 113 broad line AGN and 108 optically obscured AGN.

4.1. Luminosities

A key ingredient to estimate rest frame 2-10 keV, absorption corrected, luminosities is the shape of the X-ray spectrum. The discussion of the detailed X-ray properties of the HELLAS2XMM sources is beyond the purposes of this paper and will be presented in future publications (Baldi et al. in preparation, Perola et al. in preparation). Nevertheless, a softness ratio, defined as $(S-H)/(S+H)$, where S and H are the 0.5-2 keV and 2-10 keV fluxes respectively, can be used to derive reliable assumptions about the spectral shape. Lower values of the softness ratio indicate hard spectra; note that a value of -1 is by definition an absolute minimum of this quantity.

Fig. 2 shows $(S-H)/(S+H)$ as a function of the 2-10keV flux for the combined sample. At all fluxes from 10^{-15} to 10^{-13} erg cm $^{-2}$ s $^{-1}$ $(S-H)/(S+H)$ appears to span a very large range of values, which could hardly be accounted for by statistical uncertainties on each value, although this in some cases can be as large as 0.4-0.5. Furthermore, the thick crosses, which represent the median with the quartile range in three flux intervals, show a general trend in the spectral shape, which becomes harder as the flux decreases (see e.g. Giacconi et al. 2002 and references therein). If the spectrum is parameterized as a single power law with energy index α_E ($F(E) \propto E^{-\alpha_E}$) it is straightforward to convert $(S-H)/(S+H)$ into the slope α_E , and indicative values are given on the right axis in Fig. 2. We note that this is not a completely self-consistent procedure, because fluxes in the two bands were obtained assuming a given spectral shape (Baldi et al. 2002). However, because the width of the energy bands is small, $\lesssim 0.7$ decades, the conversion factors between count rates and fluxes depend little on the spectral shape assumption. For example the conversion factors change by 15% and 6% for a $\Delta\alpha = 0.5$ in the 2-10 keV and 0.5-2 keV bands respectively. This is much smaller than the typical statistical errors on $(S-H)/(S+H)$ and than the spread in $(S-H)/(S+H)$ in Fig. 2. If the single power law is the correct model, the points would span a very large interval in spectral slopes, from about 1.3 to -0.4 or even harder. Such a distribution is not observed in any sample of AGN, for which α_E (in the observed 0.5-10 keV band) is hardly ever outside the 1.3-0.5 range. On the other hand, photoelectric absorption would easily produce the observed softness ratios (a column density of 10^{23} cm $^{-2}$, at $z=0$, would give $(S-H)/(S+H)$ lower than -0.9 for $\alpha_E = 0.8$), and it is observed in the spectra of a large fraction of bright AGN. Furthermore, the hardening of the sources toward lower fluxes is consistent with the expectation of AGN synthesis models, which reproduce the CXB through the superposition of obscured and unobscured AGN (see e.g. Comastri et al. 2001). Our conclusion is that the wide distribution in softness ratio is unlikely to be solely due to an intrinsic dispersion of the spectral index, and that the presence of substantial absorbing columns is likely the dominant cause of its extension, especially toward values less than, say, -0.5. We have therefore decided to adopt a power law reduced at low energy by photoelectric absorption as the model used to compute the K-correction, according to the following procedure.

We assumed a power law index $\alpha_E = 0.8$ and used the observed softness ratios to estimate the column density of the absorber and therefore the unabsorbed fluxes. These unabsorbed fluxes were then used to compute rest frame 2-10 keV luminosities. The correction due to the photoelectric absorption is small in most cases ($\lesssim 10 - 20\%$ for 80-90% of the sources). For the rest of the sources having softness ratios suggesting observer frame column densities of the order of $\gtrsim 3 - 5 \times 10^{22}$ cm $^{-2}$, the correction can be of the order of a few. In a few cases the observed flux could be due to reflection, rather than to direct emission from the AGN. In these cases the real luminosities could be much higher than our estimates based on the very simple spectral model adopted. In many cases, the uncertainty on the correction can be of the same order of the correction itself, given the large errors on the determination of the softness ratio and therefore of the absorbing columns. However, since in sources with measured redshift we find no correlation between the softness ratio, and therefore the observer frame column density, and the redshift, this problem is not likely to introduce a bias in the evaluation of the evolution of the AGN luminosity function and its integrals.

On the other hand, the luminosity of all high redshift sources depends critically on the assumed X-ray spectral index. Changing the spectral index by $\Delta\alpha = 0.5$ would imply a change in luminosity of a factor of 2 at $z=3$. We shall return on this point in Sect. 6.

The redshift-luminosity diagram for the sources in the combined sample is shown in Fig. 3. It illustrates the fact that narrow beam surveys at $z < 1 - 2$ can hardly find objects of $L_X \gtrsim 10^{44}$ erg s $^{-1}$, i.e. the sources closer to the break in the Luminosity Function, which contribute most to the luminosity density at that redshift. Hence the value added by larger area surveys, such as the HELLAS2XMM survey.

5. The X-ray to optical flux ratio: the extreme X/O source population

Fig. 4 shows the X-ray (2-10 keV) to optical (R band) flux³ ratio (X/O) as a function of the X-ray flux for the four surveys. The part of the diagram below the R=25 line is accessible to optical spectroscopy with 10m class telescopes. On the other hand, the redshift of objects with $25 \lesssim R \lesssim 27$ could be determined through the comparison of their optical-NIR photometric spectral energy distribution to galaxy and AGN templates. This is also feasible with today

³ The R band flux is computed by converting R magnitudes in specific fluxes and then multiplying by the width of the R filter. We used $f_R(0) = 1.74 \times 10^{-9}$ erg cm $^{-2}$ s $^{-1}$ Å $^{-1}$ and $\Delta\lambda_R = 2200\text{Å}$, Zombeck (1990).

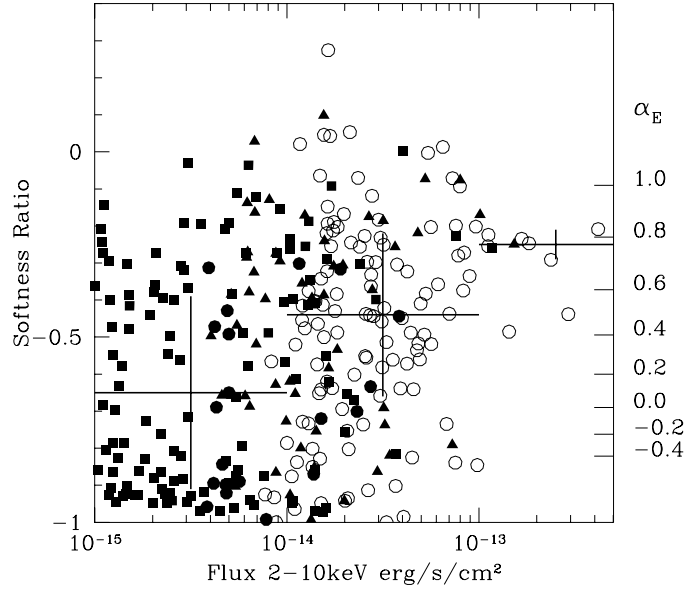


Fig. 2. The softness ratio $(S-H)/(S+H)$ ($S=0.5-2$ keV flux; $H=2-10$ keV flux) as a function of the 2-10keV flux for the sources in the combined sample (HELLAS2XMM = open circles; CDFN = filled squares; LH = filled triangles; SSA13 = filled circles). The thick crosses represent the median with the quartile range, in three flux intervals. The right axis gives the conversion from $(S-H)/(S+H)$ to α_E for a single power law spectrum.

10m class telescopes. Redshift estimate of even fainter sources must await next generation facilities like the 30-50m ground based telescopes and NGST, unless this can be done using directly the X-ray spectrum, i.e. by detecting and identifying narrow emission or absorption features.

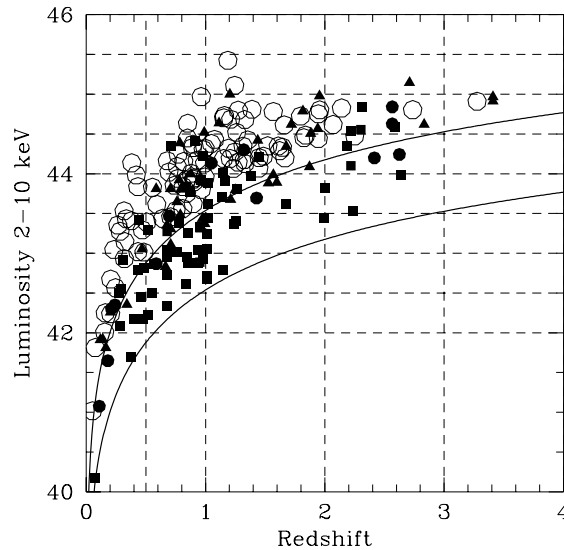


Fig. 3. The 2-10keV luminosity as a function of the redshift for the sources in the combined sample. Symbols as in figure 2. The lower and upper solid lines represent the flux limits of 10^{-15} erg cm $^{-2}$ s $^{-1}$ (i.e. Chandra deep surveys) and 10^{-14} erg cm $^{-2}$ s $^{-1}$ (i.e. HELLAS2XMM 1dF survey) respectively.

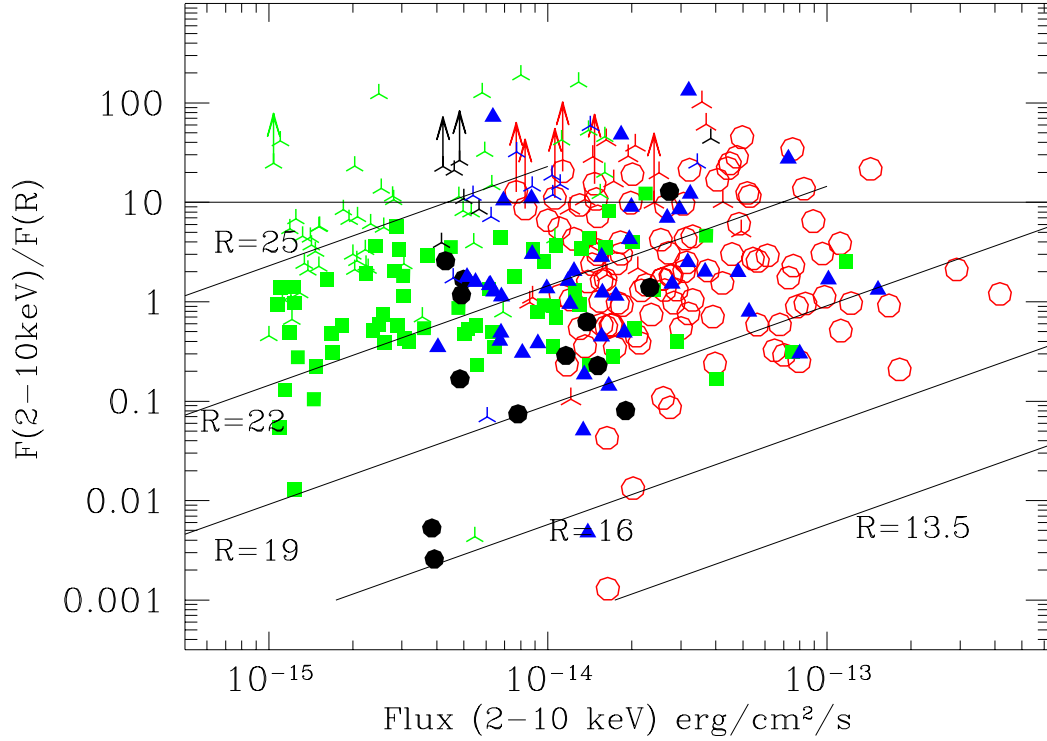


Fig. 4. The X-ray (2-10 keV) to optical (R band) flux ratio X/O as a function of the X-ray flux for the combined sample (symbols as in Fig. 2, skeleton triangles are sources without a measured redshift). Solid lines mark loci of constant R band magnitude. The part of the diagram below the $R=25$ line is accessible to optical spectroscopy with 10m class telescopes. Note as $\sim 20\%$ of the sources have $X/O \gtrsim 10$, irrespective of the X-ray flux. HELLAS2XMM 1dF sources with $X/O \gtrsim 10$ have $R=24-25$, and therefore their redshifts can be measured through optical spectroscopy.

The range of X/O spanned by X-ray sources is extremely large, up to 6 dex or even more. Indeed, one of the most intriguing results of hard X-ray surveys, is that about 20% of the sources has an X-ray to optical ratio 10 times higher or more than that typical of broad line AGN ($X/O > 10$ in Fig. 4, while typical PG QSO and Seyfert 1 galaxies have $X/O \sim 1$, see also Alexander et al. 2001). The ratio between the optical to X-ray optical depth, in the observer frame, scales roughly as $(1+z)^{3.6}$, because dust extinction increases in the UV while X-ray absorption strongly decreases going toward the high energies. The net result is that in the presence of an absorbing screen the observed optical flux of high- z QSO can be strongly reduced, and the observed magnitudes can be mainly due to starlight in the host galaxies. Conversely, the 2-10 keV X-ray flux can be much less reduced. Many extreme X-ray to optical ratio sources could then be distant, highly obscured QSO, i.e. type 2 QSO.

At the flux limit of the HELLAS2XMM 1dF survey ($F_{2-10keV} \sim 10^{-14}$ erg cm $^{-2}$ s $^{-1}$) the depth of the optical photometry and spectroscopy allows the identification of sources with $X/O \sim 10$. Conversely, most of the $X/O \gtrsim 10$ objects from ultra-deep Chandra and XMM-Newton surveys (e.g. CDFN, CDFS) have $R > 25$ and therefore are not accessible to optical spectroscopy and require ultra-deep optical photometry. The paucity of type 2 QSO among the identified sources in these surveys might therefore be partly due to a selection effect.

Among the 310 sources from the three samples considered here there are 65 sources with $X/O > 10$ (21%), 28 of them come from the HELLAS2XMM 1dF survey, and we have obtained reliable VLT spectra of 13 of them (46%). This has to be compared with the 9 out of 38 identifications in the CDFN, SSA13 and LH samples (including 3 photometric redshift of faint optical sources in the LH sample). Among the 13 identified $X/O > 10$ HELLAS2XMM sources we find 8 type 2 QSO, based on the absence of broad optical lines and their high X-ray luminosity ($L_{2-10keV} > 10^{44}$ erg s $^{-1}$). We also find 4 broad line QSO. The remaining source has an optical spectrum typical of a narrow emission line galaxy and has an X-ray luminosity of $L_{2-10keV} = 7 \times 10^{43}$ erg s $^{-1}$.

Table 2 gives the total number of sources and the number of spectroscopic identification in two flux intervals ($F_{2-10keV} = 10^{-15} - 10^{-14}$ erg cm $^{-2}$ s $^{-1}$ and $F_{2-10keV} \gtrsim 10^{-14}$ erg cm $^{-2}$ s $^{-1}$) and in three bins of X/O (> 10 ; 3-10; 0.1-3). 11 sources have $X/O < 0.1$.

Table 2. Number of sources per bins of flux and X/O ratio

| X/O | $F_{2-10keV} < 10^{-14}$ erg cm $^{-2}$ s $^{-1}$ | | | $F_{2-10keV} > 10^{-14}$ erg cm $^{-2}$ s $^{-1}$ | | |
|---------|---|-----|--------|---|-----|--------|
| | Tot. | Id. | compl. | Tot. | Id. | compl. |
| > 10 | 22 | 1 | 5% | 43 | 19 | 44% |
| 3 – 10 | 29 | 7 | 24% | 36 | 30 | 83% |
| 0.1 – 3 | 72 | 54 | 75% | 97 | 94 | 97% |

Notably, both above and below 10^{-14} erg cm $^{-2}$ s $^{-1}$ the number of objects with X/O > 3 is comparable to that of those with X/O=0.1-3. But if we consider the degree of completeness in the identifications, thanks to the HELLAS2XMM 1dF survey, it is much higher above 10^{-14} erg cm $^{-2}$ s $^{-1}$, than below.

At this point we could proceed immediately to estimate lower limits to the number density of AGN, irrespective of their type, using only the fraction of them with available redshifts. As just noted, however, this fraction is not equally representative of the whole in different bins of X/O and flux. As we shall show in the next Sect., a very different behaviour of the X/O versus $L_{2-10keV}$ is found in AGN1 and in the rest of the population. These behaviours give the opportunity to statistically attribute a distance also to the sources without a redshift determination, hence for the main purpose of this paper the whole sample could be treated as if it were completely identified.

5.1. Optically obscured vs. optically unobscured AGN

Table 3 gives for the same bins of X/O and flux of Table 2 the ratio between optically obscured to optically unobscured AGN. Although the errors on the ratios are large, a trend toward a higher fraction of optically obscured objects is suggested going both toward higher X/O values and toward lower fluxes. In order to confirm these trends one should perform a wide (≈ 1 deg 2) and deep ($F_{2-10keV} > 1 - 3 \times 10^{-15}$ erg cm $^{-2}$ s $^{-1}$) X-ray survey. To extend the redshift determinations to the sources with X/O=3-30 at this flux limit (i.e. at R=25-27) deep optical to near infrared follow-ups are needed, to obtain reliable photometric redshifts. We also note that Fig. 2 suggests, at least qualitatively, the same kind of trend, i.e. an average increase of obscuration (directly in the X-rays band in this case) going toward low fluxes.

Table 3. Ratio of optically obscured to optically unobscured AGN

| X/O | $F_{2-10keV} < 10^{-14}$ erg cm $^{-2}$ s $^{-1}$ | $F_{2-10keV} > 10^{-14}$ erg cm $^{-2}$ s $^{-1}$ |
|---------|---|---|
| > 10 | - | $3.8^{+3.2}_{-2.0}$ |
| 3 – 10 | $2.5^{+3.7}_{-2.0}$ | $1.1^{+0.5}_{-0.4}$ |
| 0.1 – 3 | $1.21^{+0.36}_{-0.30}$ | $0.31^{+0.09}_{-0.07}$ |

Fig. 5 show the X-ray to optical flux ratio as a function of the X-ray luminosity for broad line AGN (left panel) and non broad line AGN and galaxies (right panel).

The average X/O for the 113 broad line AGN of the combined sample is 1.2 with a standard deviation of 0.3. The average X/O of optically selected QSO is 0.3, with a standard deviation of 0.4, using the ASCA and BeppoSAX fluxes (George et al. 2000, Mineo et al. 2000) of 35 PG QSO. The difference in the average is due to the fact that optical selection produces a tail toward low X/O: $\sim 15\%$ of the optically selected QSO are very X-ray faint, see Laor et al. (1997), having X/O < 0.1, against $\sim 1\%$ for the broad line AGN in the combined sample.

The right panel of Fig. 5 shows the X-ray to optical flux ratio as a function of the X-ray luminosity for optically obscured AGN. There is here a striking correlation between X/O and $L_{2-10keV}$: higher luminosity AGN tend to have higher X/O. The solid diagonal line in the panel represents the best linear regression between $\log(X/O)$ and $\log L_{2-10keV}$ (a least square fit gives a slope slightly flatter than this regression). A very similar correlation is obtained computing the ratio between the X-ray and optical luminosities, instead of fluxes (because the differences in the K corrections for the X-ray and optical fluxes are small in comparison to the large spread in X/O).

All objects plotted in the right panel of Fig. 5 do not show broad emission lines, i.e. the nuclear optical-UV light is completely blocked, or strongly reduced in these objects, unlike the X-ray light. Indeed, the optical R band light of these objects is dominated by the host galaxy and therefore, X/O is roughly a ratio between the nuclear X-ray flux and the host galaxy starlight flux. While the X-ray luminosity of these objects spans about 4 decades, the host galaxy R band luminosity has a moderate scatter, less than one decade, around the mean value of $10^{11} L_{\odot}$, rather independent of redshift.

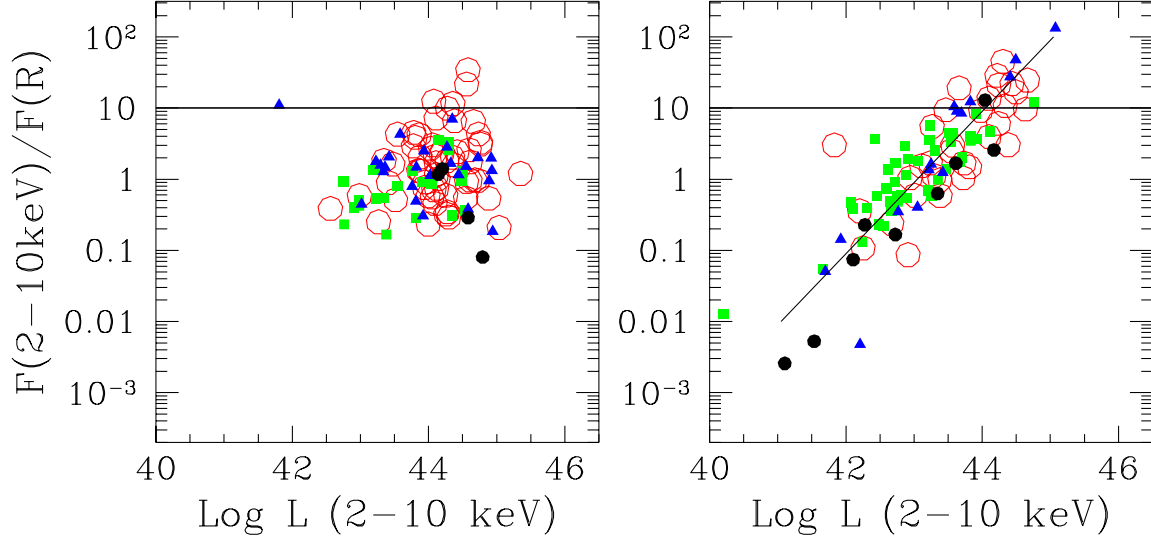


Fig. 5. The X-ray to optical flux ratio as a function of the X-ray luminosity for type 1 AGN, left panel and non type 1 AGN and galaxies (right panels). Symbols as in Fig. 2. The horizontal lines mark the level of $X/O=10$, $\sim 20\%$ of the sources in the combined sample have X/O higher than this value. The diagonal line in the right panel is the best linear regression between $\log(X/O)$ and $\log L_{2-10keV}$.

5.2. Statistical predictions for the unidentified sources

We can now use the fractions of obscured to unobscured objects in Table 3 and the correlations in Fig. 5 to predict the luminosities, and therefore the redshifts, of the sources in the combined sample without optical spectroscopic identification. The procedure is as follows: the sources without redshifts are divided in the same bins of X/O and fluxes as in Tables 2 and 3 (the few lower limits on X/O have been conservatively considered as measurements); next they are picked randomly according to the ratios in Table 3 to belong either to one or the other class. For the lower flux, $X/O > 10$ bin, for which we do not have information, we use the same ratio as in the $X/O > 10$, higher flux bin. For those falling among the optically obscured AGN we associate to each source a luminosity according to its X/O value and the linear regression drawn in Fig. 5 right panel (we note that these luminosities are slightly lower than those that would be obtained using the slightly flatter correlation given by a least square fit, see the previous Sect.). For those falling among the optically unobscured sources we associate to each source a luminosity chosen at random from a distribution similar to that of the broad line AGN in Fig. 5 left panel. From the luminosities we derive redshifts, using the same K correction and cosmology as for the sources with spectroscopic (or photometric) redshift identifications.

Because the number of objects with measured redshift in the bins with $X/O > 3$ is relatively small and therefore the errors on the ratio between obscured and unobscured objects are large, we tested several different values within the error interval. The spread introduced in the redshift and luminosity distributions by these uncertainty is smaller than 10%.

The z distribution of the 310 sources in the combined sample is plotted in Fig. 6 while the z distribution of the 132 sources in the combined sample with $F_{2-10keV} < 10^{-14}$ erg cm $^{-2}$ s $^{-1}$ is plotted in Fig. 7. The histograms of the sources with measured redshift in Fig. 7 show a sharp decrease at $z=1.2$ (similar results are presented also by Franceschini et al. 2002 and Hasinger 2003). When the sources with an estimated redshift are added, the peak of the redshift distribution at $z \sim 1$ is confirmed, but the decrease above this redshift is less sharp, thus suggesting that this

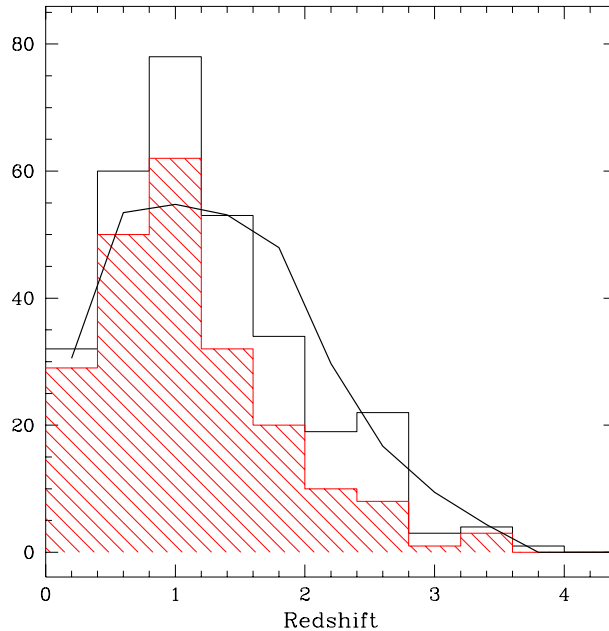


Fig. 6. The z distribution of the 310 sources in the combined sample. Shaded histogram = distribution of the spectroscopically identified sources (70 % of the sample). Solid histogram = full sample. The luminosity and the redshift of the sources without a spectroscopic redshift have been estimated using the correlation in Fig. 5, and the fraction of obscured to unobscured sources in Table 3, see Sect. 5.2 for details. The black thick line represents the expectation of the AGN synthesis models of the CXB (Comastri et al. 2001), folded through the appropriate sky-coverage, where unobscured and obscured AGN follow the same pure luminosity evolution.

feature in the distribution of the sources with spectroscopic redshift is enhanced by the incompleteness of the optical identification (in particular at high X/O values, see Table 2).

6. The evolution of hard X-ray selected sources

We have used the combined sample of 310 hard X-ray selected sources, plus 66 sources from the HEAO1 A2 all sky survey (Grossan et al. 1992) with $F_{2-10keV} > 2 \times 10^{-11}$ erg cm $^{-2}$ s $^{-1}$, to compute the evolution of the number density and of the X-ray luminosity density. We have adopted the standard $1/V_{max}$ method (Schmidt 1968, Lilly et al. 1995, Cowie et al. 2003). While it is well known that this method is not free from biases (the main one is that it does not take into account for evolution within each L and z bins), it is robust enough to derive general trends (see e.g. Cowie et al. 2003), which is the purpose of this paper. A more detailed computation of the evolution of the luminosity function using a maximum likelihood method is deferred to a future publication (La Franca et al. in preparation).

We are well aware that adopting a fixed “average” spectral index to compute the K corrections is likely to introduce a bias in both the luminosity distribution and the distribution of the maximum volume allowed at each flux limit, which will affect the evaluation of the luminosity function and its integrals (because the K correction is, roughly, a power law function of the redshift). To evaluate the magnitude of the systematic uncertainties on the luminosities and on number and luminosity densities at high z due to this bias we performed a number of dedicated simulations assuming a gaussian distribution of spectral indices with $\sigma(\alpha_E) = 0.2$, about the value found for samples of AGN bright enough to allow reliable spectral indices determinations through proper spectral fittings (see e.g. Mineo et al. 2000, George et al. 2000). We find that the number and luminosity densities at $z > 1 - 2$ obtained assuming a fixed spectral index are higher than those obtained assuming a gaussian distribution by 8-10% at most. This is smaller

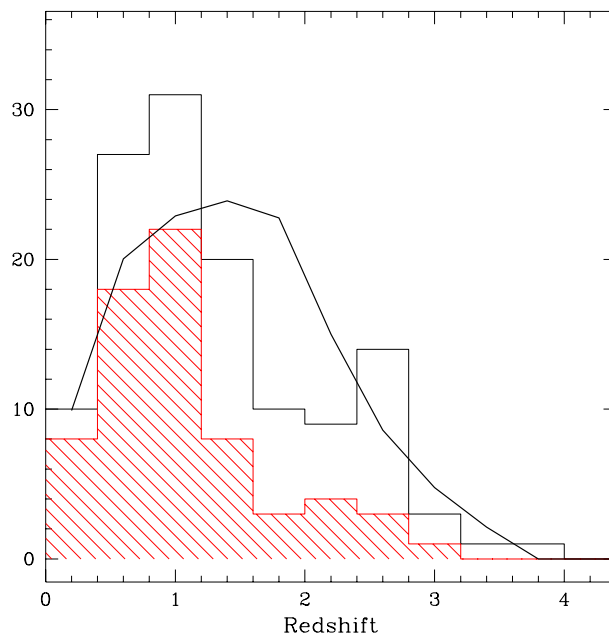


Fig. 7. The z distribution of the 132 sources with $F_{2-10\text{keV}} < 10^{-14}$ erg cm $^{-2}$ s $^{-1}$. Shaded histogram = distribution of the spectroscopically identified sources (53 % of the sample). Solid histogram = full sample. See Fig. 6 for details.

than both the statistical errors and the other systematic errors affecting such computations (see Sect. 5.2). In the following we present the results obtained using a power law spectrum with α_E fixed to 0.8 and reduced at low energy by photoelectric absorption.

We have computed the evolution of both the number density of hard X-ray sources and of the 2-10 keV luminosity density in three bins of luminosities: $43 < \log L(2-10) < 44$, $44 < \log L(2-10) < 44.5$ and $44.5 < \log L(2-10) < 46$. Fig. 8 plots the evolution of the number density for these three luminosity bins. We emphasize that the value for the $z=2-4$, $\log L(2-10)=43-44$ bin is actually a lower limit, because at our flux limit the objects with $\log L(2-10) < 43.5$ are not accessible at $z > 2$. In addition, if only the sources with a measured z are considered, we obtain the lower limits plotted as dashed lines in Fig. 8. We see that the number density of lower luminosity AGN increases between $z=0$ and $z=0.5$ by a factor ~ 13 . It stays constant up to $z \sim 2$, while at higher z we cannot obtain a reliable estimate of the number density behaviour for the reasons explained above. Conversely, the number density of luminous AGN increases by a factor ~ 100 up to $z=2$ and by a factor ~ 170 up to $z \sim 3$. The last behaviour is similar to that of luminous ($M_B < -24$) optically selected AGN (Hartwick & Shade, 1990), solid thick line in Fig. 8. The different evolution of low and high luminosity sources is confirmed if we consider the sample of the identified sources only.

Fig. 9 plots the evolution of the hard X-ray luminosity density. We see that the luminosity density of lower luminosity AGN increases from $z=0$ to $z \sim 1.5$ by a factor of ~ 18 , while that of high luminosity AGN increases up to $z=2$ by a factor ~ 100 and up to $z \sim 3$ by a factor ~ 170 .

7. Discussion and conclusions

We have obtained optical photometry and spectroscopy of a sample of 122 sources detected in the 2-10 keV band in five XMM-Newton fields of the HELLAS2XMM serendipitous survey. The number and luminosity density of AGN up to $z \sim 3$ is derived by combining ours with other samples from deeper Chandra and XMM-Newton surveys (CDFN, SSA13, Lockman Hole). The approach is rather similar to that followed by Cowie et al (2003), based on a combination

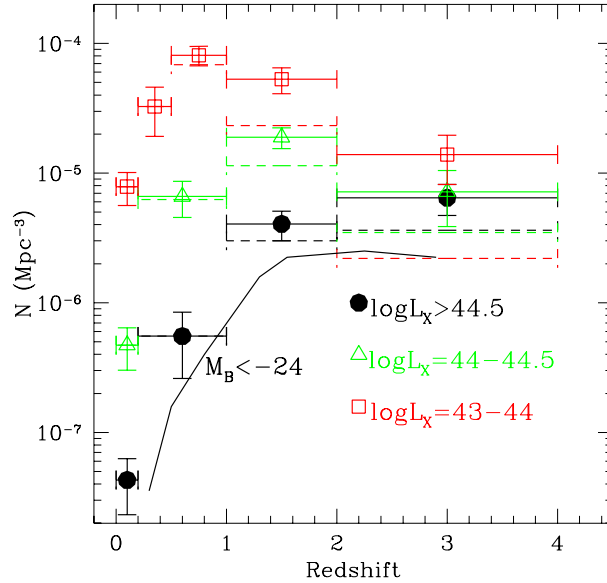


Fig. 8. The evolution of the number density of hard X-ray selected sources in three bins of luminosity: $\log L_{2-10\text{keV}} = 43-44 \text{ erg s}^{-1}$ = empty squares; $\log L_{2-10\text{keV}} = 44-44.5 \text{ erg s}^{-1}$ = empty triangles; $\log L_{2-10\text{keV}} > 44.5 \text{ erg s}^{-1}$ = filled circles. Note that the $z=2-4$, $\log L(2-10)=43-44$ bin is a lower limit, see the text for details. Dashed lines represent lower limits obtained using only the sources with measured redshift, see the text. The solid continuous curve represents the evolution of optically selected QSO more luminous than $M_B = -24$. Note as the shape of the solid curve is similar to the evolution of the luminous X-ray selected sources.

of the CDFN and a ROSAT sample. There are, however, significant differences, hence, before discussing the results, we wish to stress the major asset contributed by our medium-deep survey.

About 20% of the sources in our sample show an X-ray to optical flux ratio ten or more times higher than typical of optically selected AGN. A similar fraction of high X/O hard X-ray selected sources is also present in deeper Chandra and XMM-Newton surveys (CDFN, CDFS, Lockman Hole). At the flux limit of the HELLAS2XMM 1dF sample several sources with $X/O \gtrsim 10$ have optical magnitudes $R=24-25$, bright enough for reliable spectroscopic redshifts to be obtained with 10m class telescopes. Indeed, we were able to obtain spectroscopic redshifts and classification of 13 out of the 28 HELLAS2XMM 1dF sources with $X/O > 10$: the large majority of these sources are type 2 QSO, i.e. high luminosity ($\log L_{2-10\text{keV}} > 44$), narrow line AGN at $z=0.7-1.8$.

Conversely, at the ~ 10 times lower fluxes probed by ultra-deep Chandra and XMM-Newton surveys the optical magnitude of the sources with $X/O \gtrsim 10$ is $R \gtrsim 27$, not amenable at present to optical spectroscopy. Indeed only 9 out of the 53 sources in the combined sample with $F_{2-10\text{keV}} < 10^{-14} \text{ erg cm}^{-2} \text{ s}^{-1}$ and $X/O > 3$ have spectroscopic redshifts (and 1 among the 23 sources with $X/O > 10$, see Sect. 5 and Table 2). This limitation leads to a strong bias in ultra-deep Chandra and XMM-Newton surveys against AGN highly obscured in the optical, i.e. against type 2 QSO. In fact, only 4 type 2 QSO have been identified in the CDFN sample used in this paper (and 6 in the CDFS sample, Hasinger 2003).

This bias renders the ultra-deep surveys alone inadequate to sample properly the redshift distribution and luminosity functions. To partially (or preliminarily) overcome this problem, we have used the results obtained at higher X-ray (and optical) fluxes for the HELLAS2XMM 1dF sample to derive, with a statistical approach, an estimate of the luminosities, hence of the redshifts, of the sources in the combined sample without optical spectroscopic identification. The approach is based on: a) the fraction of optically obscured to unobscured AGN found at $F_{2-10\text{keV}} > 10^{-14}$

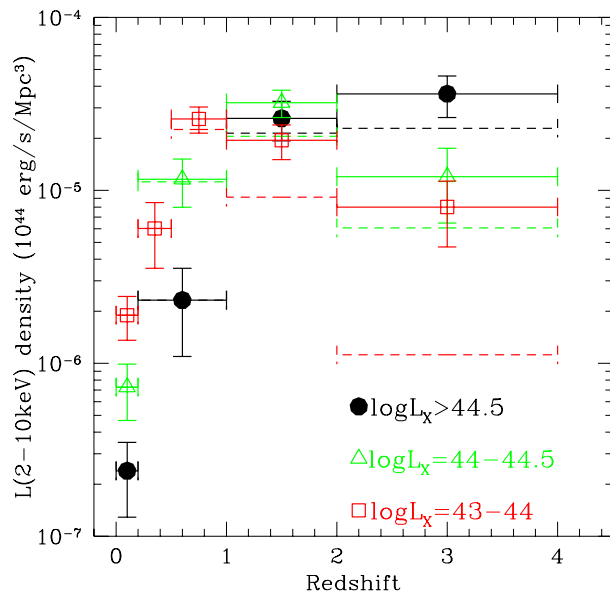


Fig. 9. The evolution of the luminosity density of hard X-ray selected sources in three bins of luminosity: $\log L_{2-10keV}=43-44 \text{ erg s}^{-1}$ = empty squares; $\log L_{2-10keV}=44-44.5 \text{ erg s}^{-1}$ = empty triangles; $\log L_{2-10keV} > 44.5 \text{ erg s}^{-1}$ = filled circles. Note that the $z=2-4$, $\log L(2-10)=43-44$ bin is a lower limit, see the text for details. Dashed lines represent lower limits obtained using only the sources with measured redshift, see the text.

$\text{erg cm}^{-2} \text{ s}^{-1}$ and $X/O > 3$; and b) the strong correlation found between the X-ray to optical flux ratio and the X-ray luminosity in obscured AGN (see Fig. 5b). It is worth noting that the X-ray to optical flux and luminosity ratios of non broad line AGN might therefore be used to investigate and constrain the relationship between the supermassive black hole masses and efficiency of accretion, and bulge optical luminosity (e.g. Gebhardt et al. 2000). This is beyond the scope of this paper and will be matter of a follow-up publication.

The combined sample of 310 sources (70% with robust spectroscopic redshifts and 30% with luminosities and redshifts assigned statistically) was then used to derive the redshift distribution and the cosmological evolution of the number and luminosity densities of accretion dominated, hard X-ray selected sources.

The redshift distributions in Fig. 6 and 7 show a clear peak at $z=1$, but, when the objects with the "estimated" redshifts are included, the drop above $z=1.2$ is rather smoother than in the plots shown in Franceschini et al. (2002) and Hasinger (2003). The solid thick curves in Fig. 6 and 7 represent the expectations from the baseline AGN synthesis models of the CXB presented in Comastri et al. (2001), where unobscured and obscured AGN, in a fixed proportion, share the same, pure luminosity cosmological evolution. Fig. 7 in particular shows that this model predicts a much broader peak between $z=1$ and $z=1.8$, falling short of the observed distribution at $z < 1$ and demanding for a slightly higher number of objects at $z=1-2$. The agreement is instead rather good at $z > 2$. The contrast does not appear as dramatic as, e.g., in Franceschini et al. (2002) and Hasinger (2003), but is telling us that at least one of the main assumptions, namely the pure luminosity evolution, which tends to broaden the peak, is not supported by the data, as definitely shown by the next step.

The evolution of high luminosity AGN ($\log L_{2-10keV} > 44.5 \text{ erg s}^{-1}$) in Fig. 8 and 9 rises monotonically from $z=0$ to $z \sim 3$ (quickly from $z=0$ to $z=1.5$ and then more gradually above this redshift). Their number and luminosity densities increase by more than two orders of magnitudes, similar to those of the high luminosity, optically selected QSO (e.g. Hartwick & Shade 1990). By contrast, the low luminosity AGN ($\log L_{2-10keV} = 43 - 44 \text{ erg s}^{-1}$) densities rise by a factor of 15-20 only, up to $z \sim 0.7$, and stay about constant up to $z = 2$. The dashed lines in Fig. 8 and

9 are lower limits computed using only the sources with spectroscopic (or photometric in three cases) redshifts. The limits are very close to the points up to $z=1$, indicating that up to this redshift our determination of the number and luminosity density of both high and low luminosity AGN is very reliable. For $z>1$ and $\log L_{2-10keV} = 43 - 44 \text{ erg s}^{-1}$ the limits are much lower than the points, which are mostly weighted by our statistical estimates. We note that points and lower limits in each luminosity bin of Fig. 8 and 9 are, by construction, all *independent*, which make them easier to compare, unlike the upper limits in Fig. 4 of Cowie et al. (2003). If our redshift estimates are correct, the number density in the $\log L_{2-10keV} = 43 - 44 \text{ erg s}^{-1}$ bin is maximal in the range $z=0.5-2$ and stays higher than that of the sources with $\log L_{2-10keV} > 44.5 \text{ erg s}^{-1}$ up to $z=3-4$ (similarly to what is found in soft X-ray selected AGN, Hasinger 2003). The luminosity density at $z < 1$ is dominated by low luminosity AGN, while (within the large statistical error bars and the uncertainty associated with the assumptions made in assigning a redshift when not directly available) at $z > 1$ those of low and high luminosity AGN are comparable, and similar to that of low luminosity AGN at $z=0.5-1$.

All these results are qualitatively in agreement with those obtained by Cowie et al. (2003). Quantitatively, we note that the integrated luminosity density we derive is higher than the value given by Cowie et al. (2003), although within their uncertainty. We obtain for $\log L_{2-10keV} > 43$ $4.6 \times 10^{39} \text{ erg s}^{-1} \text{ Mpc}^{-3}$ at $z=0.1-1$ and $5.6 \times 10^{39} \text{ erg s}^{-1} \text{ Mpc}^{-3}$ at $z=2-4$, against $\sim 2 \times 10^{39} \text{ erg s}^{-1} \text{ Mpc}^{-3}$, with a factor of ~ 3 uncertainty, in Cowie et al. in both redshift bins. This is probably due to the different prescriptions in computing luminosities (Cowie et al., 2003, do not correct for intrinsic absorption), and to the fact that deep but small area surveys probe mostly the flatter, low luminosity end of the AGN luminosity function at $z < 1 - 2$, while larger area surveys, like the HELLAS2XMM 1dF sample, push the AGN selection to 3-10 times higher luminosities (at each given $z < 1 - 2$, see Fig. 3), up to and above L^* , which identifies the break in the luminosity function, whereabouts most of the contribution to its integral comes from. We note that following the same reasoning of Cowie et al. (2003), and assuming a constant integrated luminosity density evolution, we would find a present universal supermassive black hole density of $4 - 5 \times 10^5 M_{\odot} \text{ Mpc}^{-3}$, about 2-3 times higher than that estimated by Cowie et al. (2003), but consistent with both that measured from the intensity of the CXB (Fabian et al. 1999, Elvis et al. 2002, Fabian 2003) and from local galaxies (Gebhardt et al. 2000, Ferrarese & Merrit 2000).

The qualitative picture emerging from both observational data and theories of galaxy and AGN evolution is intriguing. The evolution of luminous AGN is strong up to at least $z=2-3$ and, as suggested by e.g. Franceschini et al. (1999) and Granato et al. (2001), may follow the evolution of spheroids. Powerful AGN are likely to be present in these massive galaxies. Furthermore, the radiation and the strong winds produced by these active nuclei may help inhibiting the star-formation in these galaxies, which therefore would have red colors. Intriguingly, Mignoli et al. (2003) find a strong correlation between the R-K color and the X/O ratio for a sample of HELLAS2XMM 1dF sources. Moreover, all the 10 sources in the Mignoli et al. sample with $X/O > 10$ have $R-K \gtrsim 5$, i.e. they are all Extremely Red Objects.

On the other hand, the number and luminosity densities of lower luminosity AGN evolve up to $z=1$ and possibly decrease at $z > 2$. A similar behaviour is observed in galaxies in which the star-formation is ongoing (Lilly et al. 1995, Madau et al. 1996, 1998, Fontana et al. 1999). A link between the formation and evolution of galaxies and the growth and light-up of supermassive black holes in their nuclei has been investigated in more detail by Cavaliere & Vittorini (2000) and by Menci et al. (2003) in the framework of bottom-up models: the latter authors were able to reproduce rather naturally the steep evolution which is observed in the highly luminous quasar population. Menci et al. (2003) compare their model with the luminosity function and the number densities of luminous optically selected quasars only (since little is known about the evolution of low luminosity, optically selected AGN, because standard color techniques cannot be used when the nucleus luminosity is similar or smaller than the host galaxy luminosity). The results presented in this paper about the differential evolution of high and low luminosity X-ray selected AGN can therefore provide additional and more tight constraints to hierarchical clustering models. This will be matter of a future publication (Menci et al. in preparation).

It is clear that while the general trends are rather robust (several independent analyses converge to the similar qualitative results) the number of X-ray sources with identified redshift is still far too small to derive accurate quantitative information about the differential AGN evolution at $z=2-4$. Furthermore, the sample sizes are insufficient to attempt deriving the evolution of obscured AGN separately from that of unobscured AGN, so that key questions such as whether they are similar or not, and whether the amount of obscuration is or not related to the luminosity remain open. The above limitations can be overcome by increasing the area covered in X-ray surveys and their optical-NIR photometric and spectroscopic follow-up, both at relatively high ($F_{2-10keV} > 10^{-14} \text{ erg cm}^{-2} \text{ s}^{-1}$) and low ($F_{2-10keV} = 1 - 5 \times 10^{-15} \text{ erg cm}^{-2} \text{ s}^{-1}$) fluxes. For example, in the HELLAS2XMM 1dF sample there are some thirty "optically obscured" AGN: 100-150 sources of this type would be sufficient to adequately figure their luminosity function over 2-3 luminosity dex and a few redshift bins. This is the goal of the extension of the optical follow-up of the HELLAS2XMM survey from 1 to 4 square degree, which should allow us to contrast the luminosity function of obscured and unobscured AGN, and to study their differential evolution up to $z \sim 2$. On the other hand, the ultra-deep but small area CDFN survey has provided so far only 6 AGN more luminous than $\log L_{2-10keV} = 44$ at $z > 3$ and 20 at $z > 2$ (Cowie et al. 2003). Note that all of them have flux $\gtrsim 10^{-15} \text{ erg cm}^{-2} \text{ s}^{-1}$, suggesting that the most effective

strategy to find high luminosity, high z AGN consists in increasing the area covered at $F_{2-10keV} = 1 - 5 \times 10^{-15}$ erg cm $^{-2}$ s $^{-1}$, rather than pushing the depth of the survey. Observing ~ 0.5 square degrees of sky (roughly 10 times the area covered by the CDFN survey) at the above flux limit, would roughly increase by a factor of 10 the number of high z objects, a feasible program with a reasonable amount of observing time. The related issue of obtaining redshifts is more complex, because the optical counterparts of a large fraction of them will be too faint for optical spectroscopy. The alternative will be accurate multiband optical to near infrared photometry, in order to obtain reliable photometric redshifts through the comparison of the observed Spectral Energy Distribution with templates of galaxy and AGN spectra.

References

- Akiyama, M., et al. 2000, *ApJ*, 532, 700
- Alexander, D.M., Brandt, W.N., Hornschemeier, A.E., Garmire, G.P., Schneider, D.P., Bauer, F.E., & Griffiths, R.E. 2001, *AJ*, 122, 2156
- Baldi, A., Molendi, S., Comastri, A., Fiore, F., Matt, G., & Vignali, C. 2002, *ApJ*, 564, 190
- Banse, K., Crane, P., Grosbol, P., Middleburg, F., Ounnas, C., Ponz, D., & Waldthausen, H. 1983, *The Messenger*, 31, 26
- Barcons, X. et al. 2002, *A&A*, 382, 522
- Barger, A., Cowie, L., Mushotzky, R.F., & Richards, E.A. 2001, *AJ*, 121, 662
- Barger A., Cowie L., Brandt, W.N., Capak, P., Garnire, G.P., Hornschemeier, A.E., Steffen, A.T., & Wehner, E.H. 2002, *AJ*, 124, 1839
- Bertin, et al. 1996, *A&AS*, 117, 393
- Brandt, W.N., et al. 2001 *AJ*, 122, 2810
- Brusa, M., Comastri, A., Mignoli, M. et al. 2003, *A&A*, in press, astro-ph/0307368
- Cavaliere, A. & Vittorini, V 2000, *ApJ*, 543, 599
- Cowie L., Barger A., Bautz, M.W., Brandt, W.N., & Garnire, G.P. 2003, *ApJ*, 584, L57
- Comastri, A., Setti, G., Zamorani, G., & Hasinger, G. 1995, *A&A*, 296, 1
- Comastri, A., Fiore, F., Vignali, C., Matt, G., Perola, G. C., & La Franca, F., 2001, *MNRAS*, 327, 781
- Comastri, A. et al. 2002, *ApJ*, 571, 771
- Della Ceca, R., Castelli, G., Braitto, V., Cagnoni, I., & Maccacaro, T. 1999, *ApJ*, 524, 674
- Elvis, M., Risaliti, G., & Zamorani, G. 2002, *ApJ*, 565, L75
- Fabian, A.C., & Iwasawa, K. 1999, *MNRAS*, 303, L34
- Fabian, A.C. 2003, *Carnegie Observatories Astrophysics Series*, Vol. I, ed. L. Ho., Cambridge University Press, astro-ph/0304122
- Ferrarese, L. & Merrit, D. 2000, *ApJ*, 539, L9
- Fiore, F., La Franca, F., Giommi, P., Elvis, M., Matt, G., Comastri, A., Molendi, S., & Gioia, I. 1999, *MNRAS*, 306, L55
- Fiore, F., et al. 2000, *NewA*, 5, 143
- Fiore, F., et al. 2001, *MNRAS*, 327, 771
- Fontana, A., Menci, N., D'Odorico, S., Giallongo, E., Poli, F., Cristiani, S., Moorwood, A., & Saracco, P. 1999, *MNRAS*, 310, L27
- Franceschini, A., Hasinger, G., Miyaji, T., & Malguori, D. 1999, *MNRAS*, 310, L5
- Franceschini, A., Braitto, V. & Fadda, D. 2002, *MNRAS*, 335, L51
- Gebhardt, K., Kormendy, J., & Ho, L. et al. 2000, *ApJ*, 543, L5
- George, I.M., Turner, T. J., Yaqoob, T., Netzer, H., Laor, A., Mushotzky, R. F., Nandra, K., & Takahashi, T. 2000, *ApJ*, 531, 52
- Giacconi, R., et al. 2001, *ApJ*, 551, 664
- Giacconi, R., et al. 2002, *ApJS*, 139, 369
- Giommi, P., Perri, M., Fiore, F. 2000, *A&A*, 362, 799
- Ghizzardi, S. 2001, EPIC-MCT-TN-011
- Granato, G.L., Silva, L., Monaco, P., Panuzzo, P., Salucci, P., De Zotti, G., & Danese, L. 2001, *MNRAS*, 324, 757
- Grossan, B.A. 1992, Ph.D. thesis, MIT
- Hartwick F.D.A., & Schade, D. 1990, *ARA&A*, 28, 437
- Hasinger, G. et al. 2001, *A&A*, 365, L45
- Hasinger, G. 2003, proceedings of the Conference: The Emergence of Cosmic Structure, Maryland, Stephen S. Holt and Chris Reynolds (eds), astro-ph/0302574
- La Franca, F., Fiore, F., Vignali, C., Antonelli, A., Comastri, A., Giommi, P., Matt, G., Molendi, S., Perola, G. C., & Pompilio, F. 2002, *ApJ*, 570, 100
- Laor, A., Fiore, F., Elvis, M., Wilkes, B.J., & McDowell, J.C. 1997, *ApJ*, 477, 93
- Lehmann, I., et al. 2001, *A&A*, 371, 833
- Lilly, S.J., Tresse, L., Hammer, F., Crampton, D., & Le Fevre, O. 1995, *ApJ*, 455, 108
- Madau, P., Ferguson, H.C.L., Dickinson, M., Giavalisco, M., Steidel, C.C., & Fruchter, A. 1996, *MNRAS*, 283, 1388
- Madau, P., Pozzetti, L., & Dickinson, M., 1998, *ApJ*, 498, 106
- Mainieri, V., Bergeron, J., Hasinger, G., Lehmann, I., Rosati, P., Schmidt, M., Szokoly, G., & Della Ceca, R. 2002, *A&A*, 393, 425

- Menci, N., Cavaliere, A., Fontana, A., Giallongo, E., Poli, F., & Vittorini, V. 2003, *ApJ*, 587, L63
- Mignoli, M. et al. 2003, to be submitted
- Mineo, T., Fiore, F., Laor, A., Costantini, E., Brandt, W. N., Comastri, A., Della Ceca, R., Elvis, M., Maccacaro, T., & Molendi, S., 2000, *A&A*, 359, 471
- Mushotzky, R.F., Cowie, L.L., Barger, A.J., & Arnaud, K.A. 2000, *Nature*, 404, 459
- Oke, J.B. 1990, *AJ*, 99, 1621
- Schmidt, M. 1968, *ApJ*, 151, 393
- Schmidt, M., Hasinger, G., Gunn, J., Schneider, D., Burg, R., Giacconi, R., Lehmann, I., MacKenty, J., Trumper, J., & Zamorani, G. 1998, *A&A*, 329, 495
- Setti, G., & Woltjer, L. 1989, *A&A*, 224, L21
- Ueda, Y., Takahashi, T., Ishisaki, Y., & Ohashi, T. 1999, *ApJ*, 524L, 11
- Zombeck, M.V. *Handbook of Space Astronomy and Astrophysics*, Cambridge University Press, 1990

Table 1. The HELLAS2XMM 1dF sample

| Id | X-ray Ra 2000 | X-ray Dec 2000 | optical RA 2000 | Optical Dec 2000 | Diff. arcsec | $F_{2-10keV}$ 10^{-14} cgs | R | Class. | z | $\log L_{2-10keV}$ erg/s |
|-----------------------|------------------|-------------------|--------------------|---------------------|-----------------|---------------------------------|----------------|-------------------|-------|-----------------------------|
| 05370037 ^a | 05 41 00.4 | -28 39 05 | 05 41 00.7 | -28 39 01 | 5.8 | 4.93 | 21.5 | – | – | – |
| 05370015 | 05 40 54.3 | -28 43 45 | 05 40 54.2 | -28 43 47 | 2.4 | 3.19 | 19.9 | AGN1 | 0.880 | 44.03 |
| 05370022 ^b | 05 40 51.3 | -28 36 42 | 05 41 51.4 | -28 36 46 | 4.3 | 2.40 | $\gtrsim 23.0$ | – | – | – |
| 05370175 | 05 40 45.6 | -28 39 07 | 05 40 45.7 | -28 39 08 | 1.7 | 2.08 | 19.8 | AGN1 | 1.246 | 44.32 |
| 05370008 | 05 40 34.2 | -28 31 08 | 05 40 34.2 | -28 31 09 | 1.2 | 5.63 | 19 | ELG | 0.379 | 43.44 |
| 05370021 | 05 40 26.1 | -28 50 39 | 05 40 26.3 | -28 50 42 | 4.2 | 3.22 | 23.5 | ELG | 1.192 | 44.35 |
| 05370135 | 05 40 24.7 | -28 46 16 | 05 40 24.6 | -28 46 16 | 1.3 | 1.21 | 21.3 | AGN2 | 0.484 | 43.02 |
| 05370043 | 05 40 22.1 | -28 31 40 | 05 40 22.1 | -28 31 40 | 0.2 | 3.06 | 22.7 | AGN2 | 1.797 | 44.77 |
| 05370091 | 05 40 21.2 | -28 50 38 | 05 40 21.1 | -28 50 38 | 1.2 | 2.50 | 23.7 | – | – | – |
| 05370162 | 05 40 13.0 | -28 44 02 | 05 40 13.0 | -28 44 02 | 0.0 | 0.86 | 21.6 | – | – | – |
| 05370019 | 05 40 10.6 | -28 40 51 | 05 40 10.5 | -28 40 53 | 2.7 | 1.62 | 20.3 | AGN1 | 1.330 | 44.15 |
| 05370072 | 05 40 04.4 | -28 38 14 | – | – | – | 0.83 | $\gtrsim 24$ | – | – | – |
| 05370159 | 05 40 02.7 | -28 37 29 | – | – | – | 1.06 | $\gtrsim 24$ | – | – | – |
| 05370031 | 05 40 00.8 | -28 34 56 | 05 40 00.8 | -28 34 56 | 0.2 | 1.30 | 20.5 | AGN1 | 3.276 | 44.96 |
| 05370007 | 05 39 59.0 | -28 37 53 | 05 39 59.0 | -28 37 53 | 0.2 | 2.90 | 20.6 | AGN1 | 0.842 | 43.93 |
| 05370035 | 05 39 58.7 | -28 37 07 | 05 39 58.7 | -28 37 08 | 1.4 | 1.24 | 22.8 | AGN1 | 0.897 | 43.65 |
| 05370157 | 05 39 58.6 | -28 41 26 | – | – | – | 0.77 | $\gtrsim 24.5$ | – | – | – |
| 0537042a | 05 39 57.5 | -28 49 14 | 05 39 57.2 | -28 49 14 | 3.8 | 1.39 | 21.6 | AGN1 | 1.945 | 44.48 |
| 0537042b | 05 39 58.8 | -28 49 19 | 05 39 59.0 | -28 49 19 | 2.0 | 2.10 | 21.5 | – | – | – |
| 05370013 | 05 39 57.2 | -28 51 09 | 05 39 57.0 | -28 51 08 | 2.6 | 2.54 | 22 | AGN1 | 0.901 | 43.96 |
| 05370017 | 05 39 57.0 | -28 50 28 | 05 39 56.7 | -28 50 27 | 3.9 | 2.62 | 20.7 | AGN1 | 0.904 | 43.96 |
| 05370153 | 05 39 56.1 | -28 46 22 | – | – | – | 1.13 | $\gtrsim 24.6$ | – | – | – |
| 05370012 | 05 39 52.7 | -28 47 09 | 05 39 52.8 | -28 47 09 | 1.5 | 1.49 | 22.5 | – | – | – |
| 0537052a | 05 39 50.4 | -28 33 45 | 05 39 50.4 | -28 33 45 | 0.4 | 1.11 | 21.5 | AGN1 | 1.665 | 44.24 |
| 0537052b | 05 39 51.9 | -28 33 45 | 05 39 51.8 | -28 33 45 | 1.7 | 1.36 | 23.7 | – | – | – |
| 05370004 | 05 39 49.9 | -28 38 32 | 05 39 50.0 | -28 38 32 | 1.5 | 7.02 | 18.0 | AGN1 | 0.894 | 44.39 |
| 05370054 ^c | 05 39 45.3 | -28 49 10 | 05 39 45.2 | -28 49 10 | 1.3 | 1.62 | 25.0 | – | – | – |
| 05370014 | 05 39 43.0 | -28 27 20 | 05 39 43.1 | -28 27 19 | 2.0 | 3.00 | 19.6 | AGN1 | 1.659 | 44.68 |
| 05370041 | 05 39 39.7 | -28 31 43 | 05 39 39.8 | -28 31 42 | 1.9 | 1.56 | 20.4 | AGN1 | 1.644 | 44.38 |
| 05370078 | 05 39 38.7 | -28 48 07 | 05 39 38.7 | -28 48 08 | 1.3 | 1.44 | 22.0 | AGN1 | 1.622 | 44.33 |
| 05370036 ^d | 05 39 38.7 | -28 52 49 | 05 39 39.2 | -28 52 51 | 6.9 | 5.65 | 20.6 | AGN1 | 1.329 | 44.71 |
| 05370006 | 05 39 34.8 | -28 41 16 | 05 39 34.8 | -28 41 16 | 0.1 | 2.02 | 16 | * | – | – |
| 05370060 | 05 39 33.6 | -28 35 19 | 05 39 33.7 | -28 35 20 | 2.0 | 1.72 | 23.9 | – | – | – |
| 05370003 | 05 39 29.5 | -28 49 00 | 05 39 29.4 | -28 49 00 | 1.2 | 11.21 | 18.1 | AGN1 | 0.317 | 43.55 |
| 05370024 | 05 39 25.8 | -28 44 56 | 05 39 25.7 | -28 44 54 | 2.0 | 4.57 | 21 | ETG | 0.075 | 41.82 |
| 05370010 | 05 39 25.3 | -28 32 37 | 05 39 25.4 | -28 32 36 | 1.5 | 4.24 | 22.4 | – | – | – |
| 05370002 | 05 39 23.5 | -28 42 24 | 05 39 23.5 | -28 42 23 | 0.9 | 18.21 | 16.6 | AGN1 | 1.244 | 45.14 |
| 0537011a | 05 39 20.5 | -28 37 22 | 05 39 20.5 | -28 37 21 | 0.9 | 4.76 | 23.4 | AGN2 ^e | 0.981 | 44.33 |
| 0537011b | 05 39 21.6 | -28 38 04 | 05 39 21.6 | -28 38 06 | 2.5 | 0.88 | 21.7 | – | – | – |
| 05370040 | 05 39 20.1 | -28 36 37 | 05 39 20.1 | -28 36 38 | 1.1 | 1.54 | 21 | AGN1 | 1.485 | 44.25 |
| 05370164 | 05 39 17.2 | -28 38 20 | 05 39 17.1 | -28 38 17 | 3.3 | 1.49 | 23.6 | AGN2 | 1.824 | 44.48 |
| 05370111 ^c | 05 39 11.5 | -28 37 17 | 05 39 11.6 | -28 37 15 | 2.4 | 3.69 | 24.5 | – | – | – |
| 05370009 | 05 39 10.7 | -28 35 28 | 05 39 10.8 | -28 35 26 | 2.5 | 3.75 | 20.8 | AGN1 | 0.770 | 43.95 |
| 05370016 | 05 39 09.3 | -28 41 05 | 05 39 09.4 | -28 41 45 | 1.4 | 4.84 | 21.7 | AGN2 ^f | 0.995 | 44.35 |
| 05370005 | 05 39 05.5 | -28 33 17 | 05 39 05.5 | -28 33 16 | 1.2 | 8.94 | 21.1 | AGN1 | 1.158 | 44.75 |
| 05370123 | 05 38 51.4 | -28 39 49 | 05 38 51.5 | -28 39 49 | 1.4 | 7.53 | 23.1 | AGN1 | 1.153 | 44.72 |
| 05370020 | 05 38 50.9 | -28 37 57 | 05 38 50.9 | -28 37 58 | 0.8 | 5.43 | 20.7 | AGN1 | 0.763 | 44.21 |

Table 1. The HELLAS2XMM 1dF sample, continue

| Id | X-ray Ra 2000 | X-ray Dec 2000 | optical RA 2000 | Optical Dec 2000 | Diff. arcsec | F(2-10keV) 10^{-14} cgs | R | Class. | z | logL(2-10keV) erg/s |
|-----------------------|------------------|-------------------|--------------------|---------------------|-----------------|------------------------------|--------------|-------------------|--------------------|------------------------|
| 03120012 | 03 15 29.4 | -76 53 42 | 03 15 28.8 | -76 53 40 | 2.5 | 2.78 | 21 | AGN1 | 0.507 | 43.49 |
| 03120020 | 03 14 16.8 | -76 56 00 | 03 14 16.5 | -76 56 02 | 2.4 | 1.61 | 21.5 | ELG ^g | 0.964 | 43.87 |
| 03120010 | 03 14 16.4 | -76 45 37 | 03 14 16.5 | -76 45 36 | 0.7 | 2.13 | 19.6 | AGN1 | 0.246 | 42.74 |
| 03120022 | 03 13 49.0 | -76 45 59 | 03 13 49.3 | -76 46 00 | 1.3 | 2.71 | 21.6 | AGN1 | 2.140 | 44.85 |
| 03120036 ^c | 03 13 43.5 | -76 54 26 | 03 13 42.9 | -76 54 24 | 3.2 | 1.45 | 24.6 | – | – | – |
| 03120013 | 03 13 34.3 | -76 48 30 | 03 13 34.5 | -76 48 30 | 0.9 | 1.17 | 19.7 | AGN1 | 1.446 | 44.25 |
| 03120003 | 03 13 14.7 | -76 55 56 | 03 13 14.3 | -76 55 56 | 1.2 | 16.70 | 18.3 | AGN1 | 0.420 | 44.03 |
| 03120005 | 03 13 12.0 | -76 54 30 | 03 13 11.8 | -76 54 31 | 1.4 | 8.37 | 19.1 | AGN1 | 1.274 | 44.50 |
| 03120127 | 03 12 58.0 | -76 51 20 | 03 12 57.9 | -76 51 20 | 0.4 | 1.00 | 23.5 | AGN1 | 2.251 | 44.79 |
| 03120065 ^b | 03 12 52.2 | -77 00 59 | – | – | – | 1.47 | $\gtrsim 24$ | – | – | – |
| 03120006 | 03 12 54.0 | -76 54 15 | 03 12 53.8 | -76 54 15 | 0.7 | 8.28 | 22 | AGN2 | 0.680 | 44.16 |
| 03120018 | 03 12 39.3 | -76 51 33 | 03 12 38.7 | -76 51 33 | 1.9 | 2.59 | 18 | ETG | 0.159 | 42.24 |
| 03120008 | 03 12 31.2 | -76 43 24 | 03 12 31.3 | -76 43 25 | 1.1 | 1.64 | 13.7 | ETG ^h | 0.052 | 41.08 |
| 03120004 | 03 12 09.2 | -76 52 13 | 03 12 09.2 | -76 52 13 | 0.1 | 6.49 | 18.2 | AGN1 | 0.890 | 44.49 |
| 03120016 | 03 12 00.4 | -77 00 26 | 03 12 00.5 | -77 00 26 | 0.6 | 1.51 | 22.2 | ELG | 0.841 | 43.79 |
| 0312089a | 03 11 45.0 | -76 56 45 | 03 11 44.4 | -76 56 46 | 2.3 | 1.30 | 23.6 | ELG | 0.809 | 43.56 |
| 03120181 | 03 11 36.0 | -76 55 56 | 03 11 36.0 | -76 56 00 | 3.8 | 1.10 | 23.2 | ELG | 0.709 | 43.49 |
| 03120035 ⁱ | 03 11 31.8 | -77 00 36 | 03 11 31.8 | -77 00 32 | 4.3 | 1.83 | 22.0 | AGN1 | 1.272 | 44.16 |
| 03120066 | 03 11 28.2 | -76 45 16 | 03 11 29.2 | -76 45 15 | 3.7 | 1.51 | 23.1 | AGN1 ^e | 1.449 | 44.23 |
| 03120017 | 03 11 24.8 | -77 01 39 | 03 11 25.4 | -77 01 35 | 4.6 | 2.74 | 17.7 | ETG | 0.320 | 42.93 |
| 03120031 | 03 11 13.9 | -76 53 59 | 03 11 13.6 | -76 54 00 | 1.0 | 1.20 | 23.6 | – | – | – |
| 03120029 | 03 11 13.4 | -76 54 31 | 03 11 13.0 | -76 54 34 | 3.1 | 1.21 | 18.8 | – | – | – |
| 03120011 | 03 11 12.8 | -76 47 02 | 03 11 13.3 | -76 47 02 | 1.9 | 1.56 | 21.5 | AGN1 | 0.753 | 43.72 |
| 03120009 | 03 11 05.6 | -76 51 58 | 03 11 05.3 | -76 51 58 | 0.9 | 1.98 | 23.2 | AGN1 | 1.522 | 44.45 |
| 03120007 | 03 10 50.0 | -76 39 04 | 03 10 50.2 | -76 39 04 | 0.8 | 29.20 | 18.6 | AGN1 | 0.381 | 44.12 |
| 03120021 | 03 10 49.8 | -76 53 17 | 03 10 49.7 | -76 53 16 | 0.7 | 1.51 | 22.3 | AGN1 | 2.736 | 44.85 |
| 03120028 | 03 10 37.4 | -76 47 13 | 03 10 37.9 | -76 47 11 | 2.5 | 1.78 | 20.8 | ELG | 0.641 | 43.43 |
| 03120045 ^c | 03 10 19.0 | -76 59 58 | 03 10 18.9 | -76 59 58 | 0.5 | 1.94 | 24.4 | – | – | – |
| 03120002 | 03 10 15.8 | -76 51 33 | 03 10 15.9 | -76 51 33 | 0.5 | 41.70 | 17.6 | AGN1 | 1.187 | 45.50 |
| 03120124 | 03 10 01.6 | -76 51 07 | 03 10 01.7 | -76 51 08 | 1.3 | 1.41 | 22.5 | – | – | – |
| 03120501 | 03 09 52.2 | -76 49 27 | 03 09 51.0 | -76 49 23 | 5.9 | 1.36 | 20 | ETG | 0.205 | 42.22 |
| 03120014 | 03 09 51.2 | -76 58 25 | 03 09 51.4 | -76 58 26 | 1.5 | 3.97 | 18.4 | ELG | 0.206 | 42.66 |
| 03120024 | 03 09 31.7 | -76 48 45 | 03 09 32.1 | -76 48 46 | 1.8 | 1.76 | 21.8 | AGN1 | 1.838 | 44.58 |
| 03120116 | 03 09 18.5 | -76 57 59 | 03 09 18.2 | -76 58 00 | 1.1 | 2.01 | 23.9 | ELG | 0.814 ^l | 43.87 |
| 03120034 | 03 09 12.1 | -76 58 26 | 03 09 12.1 | -76 58 26 | 0.2 | 9.80 | 19.1 | AGN2 | 0.265 | 43.34 |

Table 1. The HELLAS2XMM 1dF sample, continue

| Id | X-ray Ra 2000 | X-ray Dec 2000 | optical RA 2000 | Optical Dec 2000 | Diff. arcsec | F(2-10keV) 10^{-14} cgs | R | Class. | z | logL(2-10keV) erg/s |
|-----------------------|------------------|-------------------|--------------------|---------------------|-----------------|------------------------------|------|-------------------|--------------------|------------------------|
| 26900038 | 23 59 57.2 | -25 05 43 | 23 59 57.2 | -25 05 44 | 1.4 | 2.25 | 21 | ELG | 0.904 | 43.93 |
| 26900075 ^c | 23 59 56.6 | -25 10 20 | 23 59 56.4 | -25 10 18 | 3.3 | 2.06 | 24.6 | – | – | – |
| 26900039 | 23 59 39.8 | -25 00 57 | 23 59 39.8 | -25 00 57 | 0.2 | 3.90 | 19.6 | AGN1 | 0.930 | 44.20 |
| 26900028 | 23 59 33.4 | -25 07 58 | 23 59 33.3 | -25 07 57 | 2.0 | 3.30 | 21.8 | AGN1 | 0.738 | 43.88 |
| 26900006 | 00 01 22.8 | -25 00 19 | 00 01 22.7 | -25 00 19 | 1.4 | 12.20 | 18.7 | AGN1 | 0.964 | 44.68 |
| 26900029 ^c | 00 01 11.6 | -25 12 03 | 00 01 11.5 | -25 12 6 | 3.9 | 3.56 | 25.1 | – | – | – |
| 26900010 | 00 01 06.8 | -25 08 46 | 00 01 06.8 | -25 08 47 | 1.4 | 3.08 | 21 | AGN1 | 1.355 | 44.47 |
| 26900003 | 00 01 02.4 | -24 58 47 | 00 01 02.4 | -24 58 49 | 1.7 | 11.16 | 20.3 | AGN1 | 0.433 | 43.85 |
| 26900002 | 00 01 00.2 | -25 04 59 | 00 00 59.9 | -25 05 00 | 4.2 | 14.35 | 21.9 | AGN1 | 0.850 | 44.66 |
| 26900014 | 00 00 44.3 | -25 07 38 | 00 00 44.3 | -25 07 40 | 2.2 | 1.63 | 21.6 | – | – | – |
| 26900022 | 00 00 36.6 | -25 01 05 | 00 00 36.6 | -25 01 06 | 1.0 | 3.14 | 21.2 | AGN2 | 0.592 | 43.64 |
| 26900007 | 00 00 34.6 | -25 06 19 | 00 00 34.6 | -25 06 21 | 1.7 | 1.68 | 20.3 | AGN1 | 1.234 | 44.22 |
| 26900004 | 00 00 31.7 | -24 54 59 | 00 00 31.9 | -24 54 57 | 3.6 | 7.96 | 17.7 | AGN1 | 0.284 | 43.35 |
| 26900013 | 00 00 30.1 | -25 12 14 | 00 00 29.8 | -25 12 17 | 4.9 | 1.63 | 17.5 | ETG ^h | 0.154 | 42.07 |
| 26900001 | 00 00 27.7 | -25 04 41 | 00 00 27.7 | -25 04 43 | 1.6 | 7.81 | 19.1 | AGN1 | 0.336 | 43.43 |
| 26900012 | 00 00 26.0 | -25 06 48 | 00 00 26.0 | -25 06 51 | 2.5 | 1.70 | 20.3 | AGN1 | 0.433 | 43.03 |
| 26900015 | 00 00 22.8 | -25 12 20 | 00 00 22.9 | -25 12 22 | 2.2 | 1.74 | 19.7 | AGN1 | 1.610 | 44.40 |
| 26900009 | 00 00 21.2 | -25 08 13 | 00 00 21.2 | -25 08 12 | 1.4 | 2.16 | 20.9 | AGN1 | 0.995 | 44.00 |
| 26900072 | 00 00 13.7 | -25 20 11 | 00 00 13.6 | -25 20 13 | 2.1 | 4.05 | 23 | ELG | 1.389 ^l | 45.37 |
| 26900016 | 00 00 02.8 | -25 11 38 | 00 00 02.7 | -25 11 37 | 1.5 | 2.75 | 21 | AGN1 | 1.314 | 44.37 |
| 15800002 | 00 34 19.1 | -11 59 37 | 00 34 19.0 | -11 59 39 | 2.3 | 9.64 | 20.2 | AGN1 | 0.848 | 44.49 |
| 15800012 | 00 34 18.5 | -12 08 09 | 00 34 18.5 | -12 08 09 | 0.5 | 6.79 | 18.8 | AGN2 | 0.233 | 43.04 |
| 15800011 | 00 34 15.4 | -12 08 47 | 00 34 15.5 | -12 08 45 | 2.9 | 1.84 | 20.7 | AGN1 | 2.069 | 44.69 |
| 15800062 | 00 34 13.9 | -11 56 00 | 00 34 13.8 | -11 56 00 | 1.1 | 4.49 | 23.3 | AGN2 | 1.568 | 44.80 |
| 15800025 | 00 34 10.0 | -12 11 26 | 00 34 09.9 | -12 11 32 | 5.8 | 2.56 | 21 | ELG | 0.470 | 43.37 |
| 15800019 | 00 33 57.3 | -12 00 40 | 00 33 57.2 | -12 00 38 | 1.9 | 3.12 | 21.8 | AGN2 ^e | 1.957 | 44.84 |
| 15800008 | 00 33 47.5 | -12 03 25 | 00 33 47.5 | -12 03 26 | 1.5 | 2.58 | 21 | AGN1 | 1.151 | 44.22 |
| 15800092 | 00 33 42.5 | -12 01 34 | 00 33 42.7 | -12 01 37 | 4.6 | 2.65 | 22.8 | ELG ^e | 0.993 | 44.16 |
| 15800013 | 00 33 39.6 | -12 08 26 | 00 33 39.6 | -12 08 28 | 2.0 | 1.82 | 22.3 | ELG | 1.326 ^l | 44.20 |
| 15800005 | 00 33 24.1 | -12 06 51 | 00 33 24.1 | -12 06 49 | 2.5 | 2.35 | 20.2 | AGN1 | 1.207 | 44.30 |
| 15800017 | 00 33 20.6 | -12 05 40 | 00 33 20.6 | -12 05 38 | 1.3 | 2.83 | 20.3 | AGN1 | 1.946 | 44.79 |
| 15800001 | 00 33 15.7 | -12 06 57 | 00 33 15.7 | -12 06 59 | 1.8 | 7.29 | 19.9 | AGN1 | 1.211 | 44.79 |
| 50900036 | 20 44 46.4 | -10 38 40 | 20 44 46.7 | -10 38 43 | 5.4 | 3.30 | 20.2 | AGN2 | 0.694 | 43.84 |
| 50900001 | 20 44 28.7 | -10 56 29 | 20 44 28.4 | -10 56 33 | 5.6 | 4.97 | 23.9 | AGN2 ^e | 1.049 | 44.40 |
| 50900061 | 20 44 20.5 | -10 49 04 | 20 44 20.5 | -10 49 03 | 1.6 | 4.22 | 20.4 | ETG | 0.324 ^l | 43.16 |
| 50900020 | 20 44 19.4 | -10 56 20 | 20 44 19.5 | -10 56 19 | 1.6 | 7.58 | 20.2 | AGN1 | 0.770 | 44.30 |
| 50900067 | 20 44 07.1 | -10 56 11 | 20 44 07.2 | -10 56 12 | 1.5 | 5.29 | 22.3 | AGN1 | 1.076 | 44.44 |
| 50900013 | 20 43 49.7 | -10 32 44 | 20 43 49.5 | -10 32 40 | 5.0 | 4.42 | 23.2 | AGN2 | 1.261 | 44.55 |
| 50900031 | 20 43 49.2 | -10 37 46 | 20 43 49.1 | -10 37 43 | 3.0 | 6.13 | 20.6 | AGN1 | 0.556 | 43.82 |
| 50900039 | 20 43 22.8 | -10 40 30 | 20 43 22.5 | -10 40 31 | 4.7 | 5.19 | 22.4 | AGN1 ^e | 0.818 | 44.17 |

Classification: AGN1; AGN2; ELG=Emission Line Galaxy; ETG=Early Type Galaxy; *=Star; ^a Group of galaxies in the error-box; ^b Near bright star; ^c Aperture photometry at the position of a bright K source (Mignoli et al. 2003) ^d Two possible counterparts; ^e Classification tentative; ^f Two nearby objects, a type 2 AGN and an emission line galaxy, at the same redshift; ^g Two nearby emission line galaxies at the same redshift; ^h Extended, emission from a group or cluster of galaxies, z based on nearest galaxy; ⁱ Two possible counterparts, a type 1 AGN and an R-K \gtrsim 6.1 object (Brusa et al. 2003, Mignoli et al. 2003); ^l redshift tentative, based on a single faint line.